



Subcretionary tectonics: Linking variability in the expression of subduction along the Cascadia forearc



Jonathan R. Delph ^{a,b,*}, Amanda M. Thomas ^b, Alan Levander ^c

^a Department of Earth, Atmospheric, and Planetary Sciences, Purdue University, 550 Stadium Mall Dr., West Lafayette, IN, 47907, USA

^b Department of Earth Sciences, University of Oregon, 100 Cascade Hall, Eugene, OR, 97403, USA

^c Department of Earth, Environmental and Planetary Sciences, Rice University, 6100 Main St., Houston, TX, 77005, USA

ARTICLE INFO

Article history:

Received 30 June 2020

Received in revised form 1 December 2020

Accepted 14 December 2020

Available online 6 January 2021

Editor: J.-P. Avouac

Keywords:

subduction

forearc structure

seismic imaging

orogenesis

underplating

ABSTRACT

A number of seismic and other geophysical phenomena exhibit significant lateral heterogeneity along the strike of the Cascadia forearc. Both the overriding and downgoing plate have been invoked to play the dominant role in controlling along-strike correlations between seismogenic behavior, potential field measurements, morphological/tectonic characteristics, and seismic structure; however, significant feedbacks likely exist between the two. In this study, we apply a 3D velocity correction to receiver function data and interpret the resulting discontinuity model alongside a recently published shear-wave velocity model to understand the possible causative relationships between correlative along-strike variations. Our discontinuity model indicates that the forearc crust thickens as it approaches the mantle wedge corner before progressively thinning toward the magmatic arc, likely due to the basal accretion of material from the downgoing plate to the overriding plate. In the northern and southern portions of the forearc, this "subcreted" material is characterized by thick (~10 km) anomalously low shear-wave velocity zones. The thickness, high internal reflectivity, and low Bouguer gravity signatures associated with the low velocity zones likely indicate that this subcreted material is composed of dominantly (meta)sedimentary material that has been emplaced through successive subcretion events over geologic timescales. Furthermore, the anomalously low velocities and spatial correlation with high non-volcanic tremor (NVT) density and short slow slip recurrence intervals indicate that these regions are fluid-rich. While first-order variations in the fluids that control NVT and slow slip likely result from differences in the permeability of the downgoing slab as inferred from its stress state and the distribution of intraslab seismicity, these subcreted packages likely represent thick, vertically-impermeable regions in the lower crust that further accentuate this correlation. Variability in the amount of subcretion explains patterns of exhumation and uplift along the Cascadia margin and the resulting forearc topography over geologic timescales, and is likely controlled by some combination plate interface geometry/rheology and overriding plate architecture.

© 2020 Elsevier B.V. All rights reserved.

1. Introduction

The modern Cascadia margin is a ~1200 km long subduction zone along the northwestern coast of North America that has been operating since the accretion of the Siletzia terrane at ~50 Ma (Wells et al., 2014). This margin is characterized by the subduction of the young oceanic lithosphere of the Juan de Fuca plate (5–10 Myr at the trench) at slow-to-intermediate convergence rates (between 30 and 42 mm/yr) in a northeasterly direction (Fig. 1) (Wilson, 2002). The combination of the young oceanic

lithosphere and low variations in convergence rates makes Cascadia one of the endmember examples of a warm subduction system (van Keken et al., 2011). This results in a significant amount of fluid release from the subducting lithosphere starting at relatively shallow depths (~40 km; Condit et al., 2020), which will affect the seismogenic and rheological characteristics of the plate interface. While significant variations in fluid-mediated subduction processes along the Cascadia forearc are observed, as seen in variable slow-slip recurrence intervals (Brudzinski and Allen, 2007), non-volcanic tremor (NVT) density, and intraslab seismicity (McCrory et al., 2012), the predicted depth of dehydration appears relatively invariant along-strike based on first-order characteristics of the subducting slab (Condit et al., 2020), making this an unlikely cause of the variation in seismogenic behavior. Other ob-

* Corresponding author at: Department of Earth, Atmospheric, and Planetary Sciences, Purdue University, 550 Stadium Mall Dr., West Lafayette, IN, 47907, USA.

E-mail address: jdelph@purdue.edu (J.R. Delph).

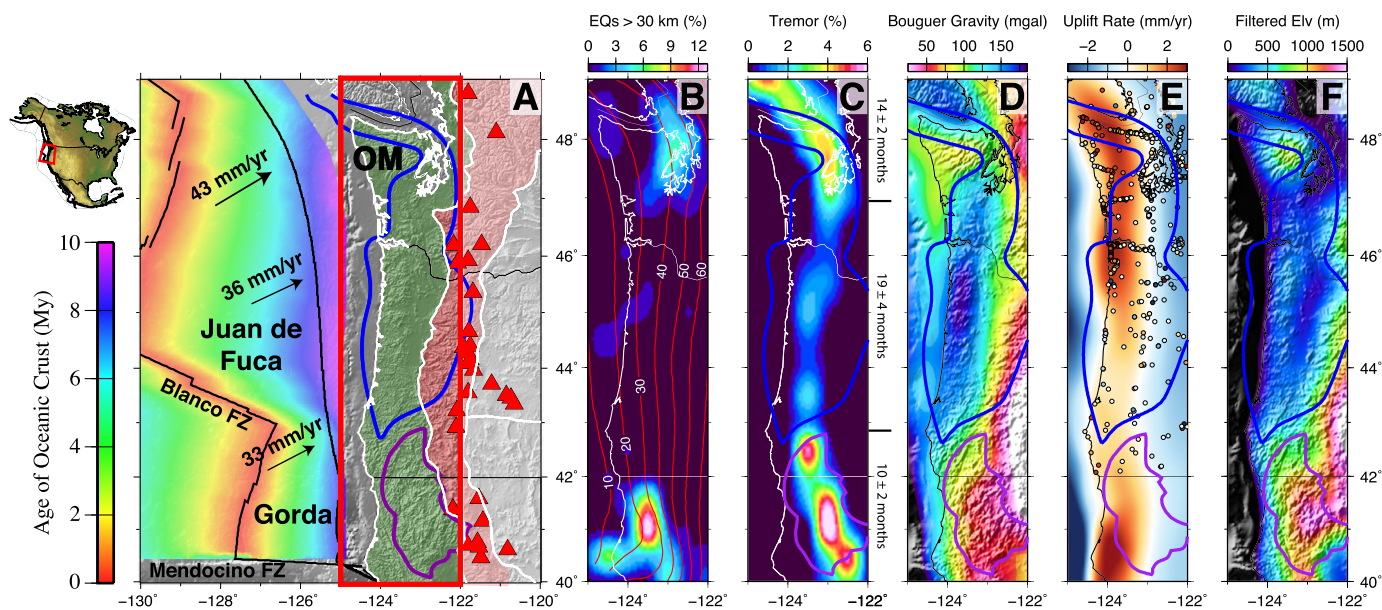


Fig. 1. Observed variability in subduction characteristics along the Cascadia forearc. (A) Subducting plate age, relative convergence, and physiographic provinces of the Cascadia margin. Green shading: onshore forearc; red shading: Cascade magmatic arc; red triangles: Holocene volcanic centers. Blue polygon: Siletzia Terrane. Purple polygon: Klamath terrane. (B) Distribution of seismicity at >30 km depth, assumed to primarily occur within the downgoing slab. (C) non-volcanic tremor density distribution (www.pnsn.org/tremor; Wech, 2010) and slow slip recurrence intervals (Brudzinski and Allen, 2007). (D) Gaussian-filtered Bouguer gravity anomaly with a σ of 25 km. (E) Predicted interseismic uplift rates from the locking model of Li et al. (2018). Circles are decadal uplift rates from GPS and tide gauges. (F) Gaussian-filtered elevation with a σ of 25 km. (For interpretation of the colors in the figure(s), the reader is referred to the web version of this article.)

servations also spatially correlate with the seismogenic behavior of the margin, which may lend insight into controls on this variation. These include crustal seismicity (Bostock et al., 2019), gravity and magnetic fields (Blakely et al., 2005), uplift and erosion rates (Balco et al., 2013; Burgette et al., 2009), topography, slab morphology (McCrory et al., 2012), intraslab deviatoric stresses (Wada et al., 2010), and interface locking (Li et al., 2018; Schmalzle et al., 2014) (Fig. 1), and are also reflected in the seismic properties of the margin, such as forearc Rayleigh wave phase and crustal shear-wave velocities (Delph et al., 2018; Janiszewski et al., 2019; Porritt et al., 2011), seismic attenuation (Littel et al., 2018), and subslab mantle structure (Bodmer et al., 2018). The significant correlations between these different observations have proven difficult to link in a mechanistic way due to their different temporal and spatial scales. However, understanding these linkages is necessary to decipher the governing factors that lead to along-strike variations in subduction characteristics not only along the Cascadia forearc, but along other subduction margins as well.

Recent studies posit the dominant controlling mechanism behind the distribution of NVT in Cascadia is related to either the properties of the overriding or downgoing plate. For instance, NVT distribution has been related to overriding plate structure through variations in either: 1) the permeability of the overriding crust due to the presence of vertically extensive forearc faulting (Wells et al., 2017), or 2) the strength of the overriding plate implied from surface geology (Fig. 1A; Brudzinski and Allen, 2007). While these explanations likely contribute to distribution of NVT and could plausibly be related to variations in topography and Bouguer gravity along the margin, it is unclear how it would contribute to other phenomena that correlate with NVT, such as intraslab seismicity (Fig. 1B) and upper mantle velocity structure (Bodmer et al., 2018). Alternatively, buoyancy variations in the upper mantle below the subducting oceanic lithosphere have been invoked as the primary control on plate locking, and perhaps also uplift, and exhumation, by controlling slab curvature and thereby modulating changes in both along-strike and down-dip friction of the interface (Bodmer et al., 2018, 2020). This hypothesis could also be linked with intraslab seismicity, but its connection with variations in NVT and over-

riding crustal characteristics, such as Bouguer gravity variations, crustal seismic properties, or surface geology, are difficult to explain. Delph et al. (2018) attempted to link slab structure with NVT distribution by inferring that intraslab seismicity reflected permeability changes within the downgoing slab, leading to variable fluid release from the downgoing slab. The regions of high NVT density also coincided with thick low velocity zones interpreted as underplated sedimentary packages below the forearc, perhaps resulting from intrinsic vertical impermeability of the material. However, no controlling mechanism for the variable amounts of underplating was presented.

In this study, we provide plausible mechanistic linkages between the seismic structure of the Cascadia margin and other margin characteristics. We leverage the existing dense station distribution along with a recently published 3D shear-wave velocity model (Delph et al., 2018) and a new variable Vp/Vs ratio crustal model derived from local seismicity to convert P-wave receiver functions to depth. The resulting 3D velocity-corrected discontinuity model better delineates the seismic discontinuity structure of the Cascadia margin and allows for the systematic estimation of crustal thickness, which has proven difficult in previous studies due to the complexity of the crust-mantle transition in subduction zones (e.g., Bostock, 2013). This new 3D discontinuity model in combination with our previously computed 3D model of shear-wave velocities allows us to investigate how the seismic structure of the margin relates to lateral variations in subduction characteristics.

2. Methods

Receiver functions are commonly used to locate the crust-mantle transition and delineate the discontinuity structure beneath a region, as their peaks and troughs directly correspond to velocity increases and decreases in the Earth. However, delineating the crust-mantle transition in Cascadia has been challenging due to: 1) the difficulty of differentiating between the base of the overriding crust and the downgoing plate's crust in the forearc where they are in contact, as they are both primarily composed of mafic

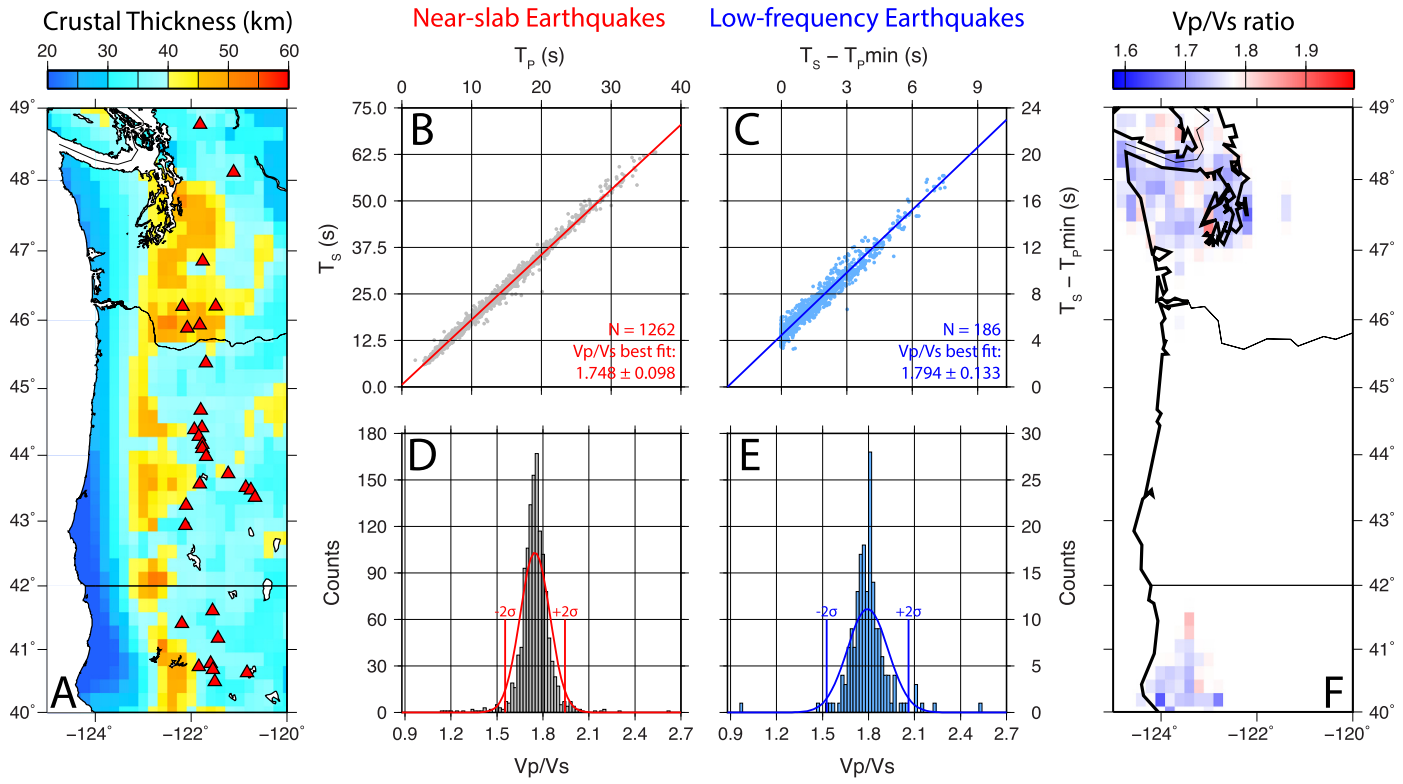


Fig. 2. Constraints for building the variable Vp/Vs ratio 3D velocity model. (A) Map of overriding plate crustal thickness along the Cascadia margin. (B, C) Wadati diagrams for earthquakes and LFEs. LFE x-axis normalized to first arrival of P-wave from an event. (D, E) Resulting distribution of estimated Vp/Vs ratios from individual earthquakes and LFEs. (F) 0.2×0.2 spatially-averaged map of Vp/Vs ratios from LFEs and earthquakes. Areas that could not be constrained by Wadati diagrams are set to a Vp/Vs of 1.78 (white background).

material, and 2) pervasive serpentinization of the mantle wedge beneath much of the Cascadia forearc (e.g., Brocher et al., 2003), resulting in very small velocity contrasts across the crust-mantle transition (e.g., Bostock, 2002, 2013; Abers et al., 2017; Crosbie et al., 2019). In an attempt to mitigate these issues, we created a 3D model of P-wave radial receiver function conversion amplitudes using adaptive common conversion point stacking (ACCP; Delph et al., 2015, 2017) alongside a 3D velocity model correction. This velocity correction involves combining a previously derived 3D shear-wave velocity model (Delph et al., 2018) with a 2D model of Vp/Vs ratio for the crust. This 3D variable Vp/Vs ratio velocity model was made using 1): the slab top model of McCrory et al. (2012), 2) an estimate of crustal thickness based on the shear-wave velocity model of Delph et al. (2018), and 3) an estimate of crustal Vp/Vs ratios derived from local body-wave travel times of near-slab seismicity. Details of the shear-wave velocity model creation, including the dataset, receiver function computation, and ambient noise methodology are detailed in the supplementary material of Delph et al. (2018) and only briefly explained below as relevant to new data. Here, we describe the creation of the 2D Vp/Vs ratio surface for the Cascadia crust that was incorporated with the 3D shear-wave velocity model to create a 3D, variable Vp/Vs ratio velocity model.

2.1. 3D variable Vp/Vs ratio velocity model creation

The 3D shear-wave velocity model was created from the joint inversion of 1 Hz P-wave radial receiver functions and 8–50 second ambient noise-derived Rayleigh wave dispersion data using a non-linear least-squares inversion (Julià et al., 2000). We used this shear-wave velocity model to estimate initial crustal thickness throughout the study area by assuming the uppermost mantle has a minimum velocity of ~ 4.2 km/s. This velocity is a lower bound

for unaltered peridotite (McCarthy et al., 2011) and is faster than what would be expected for most crustal compositions (e.g., Christensen, 1996). Based on comparison with the ACCP stacks using a 1D velocity model (Delph et al., 2018; also shown in Figs. S2F, S3F, S4F), this velocity also generally corresponds to the maximum receiver function amplitude at depth, which usually represents the Moho in areas where the lithospheric structure is relatively simple. If shear-wave velocities did not reach 4.2 km/s at depths shallower than the estimated top of the slab from McCrory et al. (2012), we set the overriding plate crustal thickness as the depth to the top of the slab. Above the forearc mantle wedge, pervasive serpentinization resulting in antigorite formation can decrease shear velocities in peridotite from ~ 4.5 to < 4.0 km/s (Christensen, 2004; Crosbie et al., 2019), causing the conversion at the Moho discontinuity to be very low amplitude, as a shear velocity of ~ 4.0 km/s is consistent with some lower crustal lithologies (Christensen, 1996). Therefore, where not clearly visible, the Moho was manually interpolated from the nearby grid points to follow the 4.0 km/s velocity contour, the slowest expected for a fully serpentinized mantle based on the Hashin-Strickmann approximation calculated for appropriate P-T conditions (Crosbie et al., 2019). The resulting crustal thickness model is shown in Fig. 2A. Uncertainties in the depth to the base of the crust are ± 5 km based on the plausible range of bulk crustal Vp/Vs values and the differential smoothing operator applied in the joint inversion for shear-wave velocity.

As the timing of arrivals in receiver functions is dependent on Vp and Vs, which is rarely uniform at a regional scale, estimating the Vp/Vs ratio throughout our study area is necessary to create an accurate model of velocity discontinuities. To obtain estimates of crustal Vp/Vs ratio in the Cascadia forearc, we analyzed travel times from low frequency earthquakes (Royer and Bostock, 2014) and seismicity occurring within 5 km of the slab model from McCrory et al. (2012) (Fig. 2B–E). A linear regression was applied to

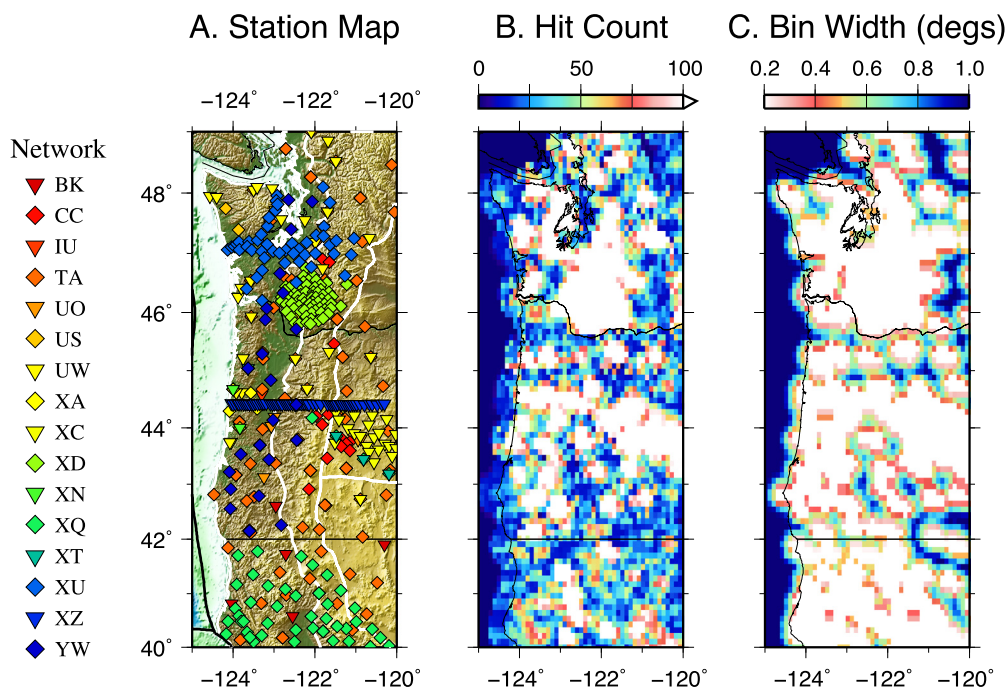


Fig. 3. Map of stations that contributed P-wave receiver functions to the ACCP model (A), alongside bin width (B) and hit count (C) at 40 km depth in the model. Network descriptions and references in Supplemental Table S2.

events with more than 4 reported P and S travel times, and any results with an $R^2 < 0.9$ were discarded. We also discarded any measurements outside of the 2σ bounds of the resulting distributions and discretized the study area into $0.2^\circ \times 0.2^\circ$ bins to match the spatial discretization of the Vs model. If multiple events occurred within a given bin, the Vp/Vs ratio results were averaged for that bin. Any bin that contained ≤ 1 event was set to have a Vp/Vs ratio of 1.78, which is appropriate for a crust of bulk intermediate composition (Christensen, 1996). The resulting Vp/Vs ratios (Fig. 2F) were then used to convert Vs from the 3D shear-wave velocity model to Vp in the crust at the associated location. Interestingly, some variability in the estimated Vp/Vs ratios between LFEs and earthquakes were found (Fig. S1), however due to the lack of LFEs elsewhere along the margin that could be used to estimate the Vp/Vs ratio, we averaged the results from the two datasets. At depths greater than the estimated overriding plate crustal thickness (Fig. 2A), the Vp/Vs ratio was assumed to be 1.78 based on IASP91 (Kennett and Engdahl, 1991). While large, local variations in Vp/Vs ratios have been inferred in thin layers near the subduction interface (e.g., Audet et al., 2010), their effect on mean crustal Vp/Vs ratios is small.

2.2. Receiver functions and adaptive CCP stacking

The receiver function dataset from Delph et al. (2018) was supplemented with data from the iMUSH broadband deployment for this study, which consisted of an additional ~ 2 yrs of data from 70 stations centered around Mt. St. Helens (Creager, 2014) (Fig. 3a; network XD). The combined dataset consists of 94,218 P-wave radial receiver functions from 1,080 stations. We only focus on the model between 40° to 49° N and -125° to -120° in this study. Receiver functions were computed following the same approach as in Delph et al. (2018), which involved 1) obtaining data for $Mw \geq 5.5$ earthquakes at epicentral distances between 30° – 95° , 2) filtering the data between 0.05–4 Hz and visually inspected the vertical component to ensure a clear P-wave arrival for each event, 3) rotating the data into the Z-R-T domain prior to performing time-domain iterative deconvolution with a 2.8 Gaussian

parameter to calculate P-wave radial receiver functions (Ligorria and Ammon, 1999), and 4) performing a visual check on the resulting receiver functions. The iterative deconvolution was terminated after either 800 iterations or there was a <0.001 improvement in the RMS misfit. The end result was the addition of 7,873 receiver functions from the iMUSH deployment to the dataset of Delph et al. (2018).

To create a common conversion point (CCP) stack (Dueker and Sheehan, 1997), a region is discretized into a 3-dimensional model defined by a bin spacing (lateral step), a bin width (lateral smoother), and a bin height (vertical step). Receiver function sampling locations are then computed via ray tracing through the model assuming a (commonly 1D) velocity structure and converted to depth. All receiver function segments that fall into the same bin are averaged to create a continuous model of discontinuities beneath the study area. We apply two modifications that increase the spatial resolution of this approach: 1) we apply a 3D correction from the model described in the previous section that accounts for variations in velocity structure following the approach of Eagar et al. (2010), and 2) we allow bin size to adapt to ray density within a given bin (adaptive CCP, or ACCP, stacking).

For our ACCP stacking model, we use a bin spacing of 0.1° , a bin height of 0.5 km, and a minimum bin width of 0.2° that expands in increments of 0.1° up to 1° if < 10 receiver functions are in a bin (e.g., Fig. 3B,C). We calculate the conversion locations for each depth for all receiver functions based on a simplified 1D velocity profile characterized by a Vp of 6.6 km/s at depths < 38 km based on the average crustal velocity of Moran et al. (1999) and 8.01 km/s at depths $> = 38$ km with an assumed Vp/Vs ratio of 1.78 throughout (Table S1). We then use our 3D velocity model to convert receiver function times to depth based on the velocity structure along the computed 1D raypath, resulting in a compaction/dilation of the receiver function time series compared to the 1D model. It is not necessary to calculate new conversion locations using the 3D velocity model for the Ps phase as variations will be < 5 km for even the most extreme velocity variations at depths < 100 km, which is less than the minimum bin-width of the ACCP stacks. Alongside the variable Vp/Vs ratio velocity model, we

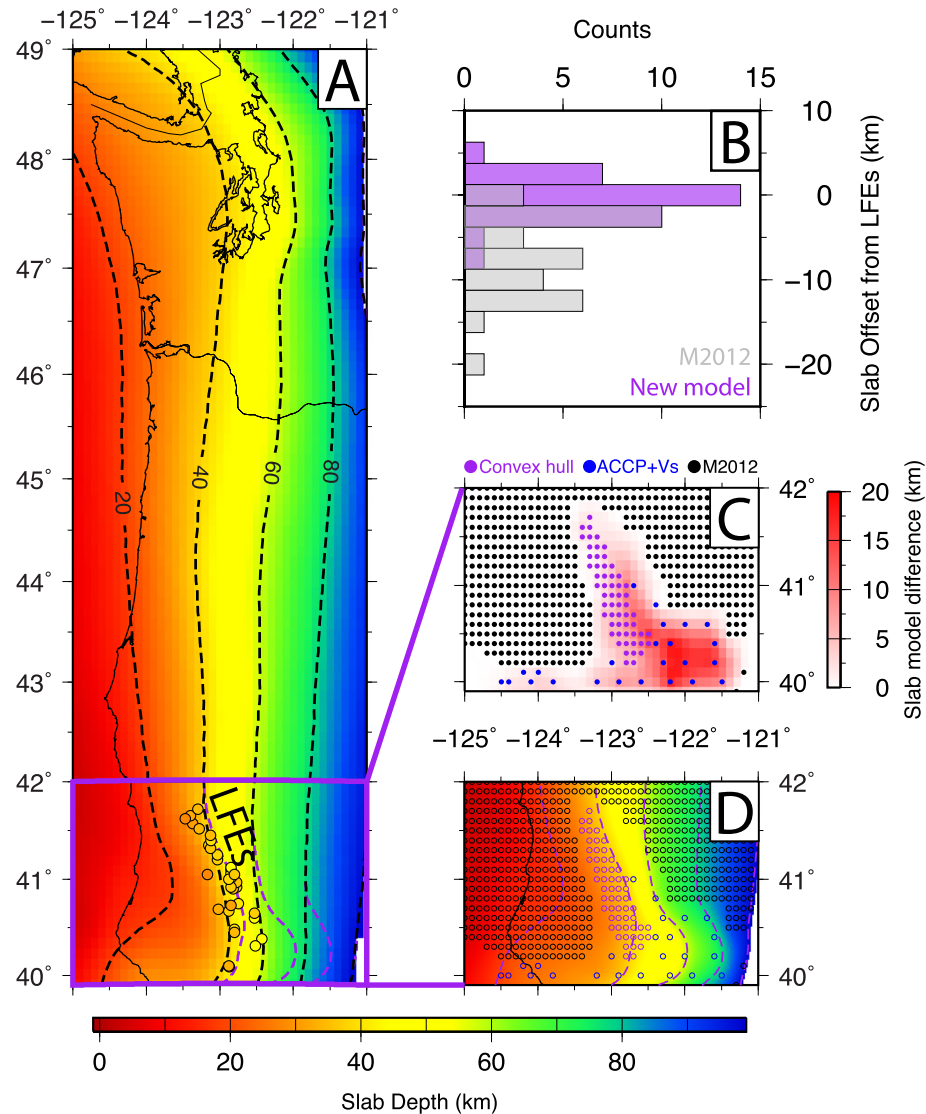


Fig. 4. Comparison between slab models. (A) Model of McCrory et al. (2012) colored by depth. LFE locations shown by circles and colored by depth (Plourde et al., 2015). Contours every 20 km. Purple line: refined slab model from this study. (B) Histogram of differences between LFE locations and slab depth at their epicenter (gray, McCrory et al., 2012; purple, refined slab model). The M2012 model is often >5 km deeper than LFE hypocenters, while the modified slab model is in much better agreement with LFEs. (C) Modification to the M2012 model (black dots) using a surface created with a 3rd order polynomial fit constrained by a convex hull around LFE hypocenters (purple dots). This surface was merged smoothly with the M2012 model through visual comparison with the ACCP and Vs models (blue dots). (D) Modified slab model in southern Cascadia. Circles are control points in (C).

also created ACCP stacks with a 3D velocity correction assuming constant crustal V_p/V_s ratios of 1.7, 1.78, and 1.9 for comparison (Figs. S2–S4).

2.3. Slab model adjustments

Low frequency earthquake (LFE) hypocenters in northern California (Plourde et al., 2015) alongside intraslab seismicity indicate that existing models of the subduction interface (e.g., McCrory et al., 2012; Hayes et al., 2018; hereafter referred to as M2012 and Slab2) are locally in error (Fig. 4). NVT is likely composed of small LFEs, which are thought to take place at or near the plate interface based on its spatiotemporal correlation with geodetically observed slow slip and moment tensors consistent with plate boundary slip (e.g., Shelly et al., 2007). Therefore, LFE hypocenters may represent the best estimate of the depth to the plate interface. We use LFE locations alongside our seismic images to modify the M2012 slab model in southern Cascadia, as the M2012 model appears to agree

better with seismic images and earthquakes in Cascadia than the Slab2 model for this region.

To modify the slab location, we fit a 3rd order polynomial to LFE locations from Plourde et al. (2015). We then replaced points from the M2012 model with the depths to the polynomial surface in the region defined by a convex hull surrounding the LFE locations. To smoothly merge the LFE-constrained surface with the slab model and accurately constrain the depth to the slab downdip of the LFEs, the slab surface was visually modified using the remigrated ACCP stacks and shear-wave velocity model. Gaps in the final surface were interpolated using a minimum curvature interpolation. The resulting changes in the slab model are shown in Fig. 4. While uncertainty is present in both LFE locations and seismic velocity models due to a priori assumptions (e.g., velocity model used for LFE locations and ACCP model), the consistency between the seismic images and LFE locations in northern California indicated that the slab surface needed to be corrected to shallower depths. Inaccuracies in the slab model were likely based on a lack

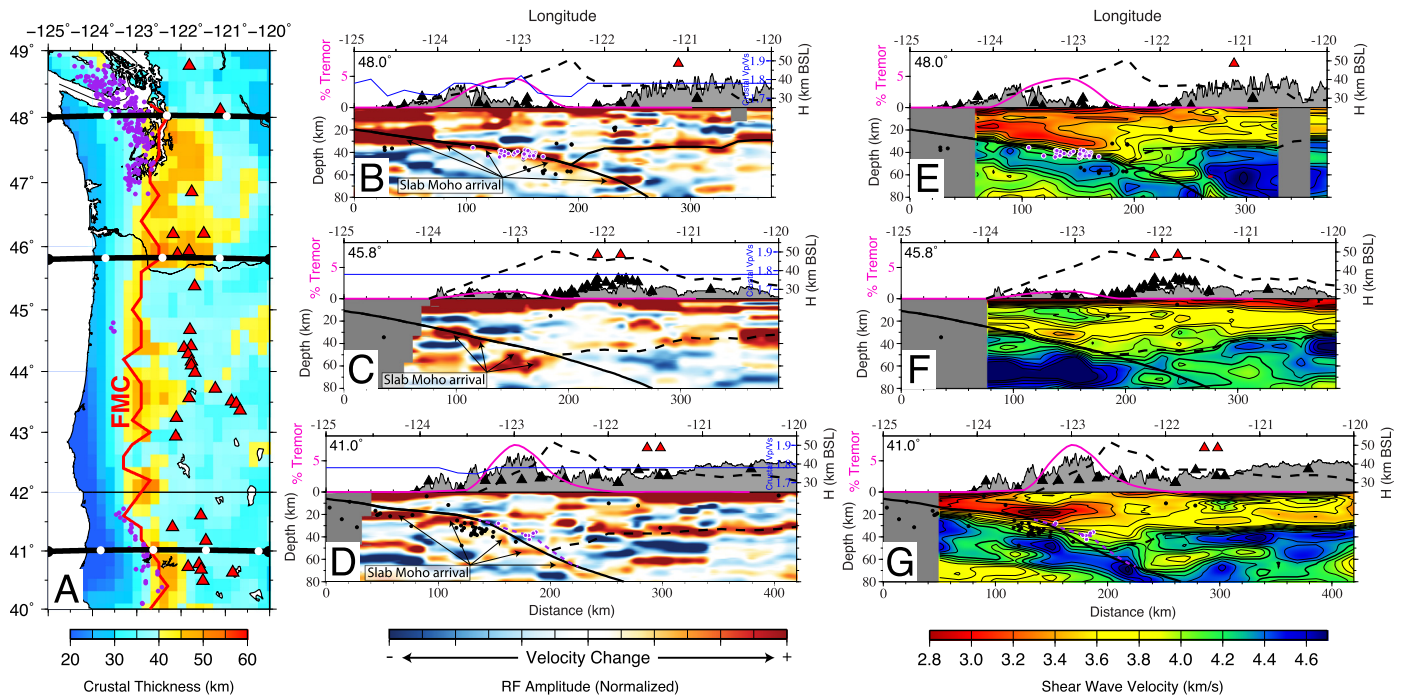


Fig. 5. Map of crustal thickness of the overriding plate along the Cascadia margin. Red line is the intersection of the overriding and downgoing crust (the “forearc mantle corner” or FMC). Thicknesses up-dip of the FMC line are constrained by the slab model of McCrory et al. (2012). A clear thickening of the overriding plate from west to east is observed in the forearc, and crustal thickness beneath the volcanic arc is generally thinner than in the forearc. Black lines with white circles correspond to cross-sections marked every 100 km. (B–G) Velocity-corrected ACCP receiver function stacks and corresponding shear-wave velocity images. Dashed black line: Moho depth; fuchsia line: tremor density at cross-section location (from Fig. 1C); blue line in (B–D), Vp/Vs ratio along cross section (Fig. 2F); gray shading, topography along cross section; black triangles, seismic stations within 10 km of these sections; red triangles: nearby Holocene volcanic centers; purple dashed line: modified slab model; black solid line: M2012 slab model; purple dots: LFE locations; black dots: earthquakes $M_w > 2.5$ from the USGS NEIC catalog.

of constraints from controlled source seismic data in the region and difficulty separating crustal from downgoing plate seismicity, and the discrepancy is largely located in regions where the crust of the two plates is in contact (i.e., before reaching the mantle wedge).

3. Results

3.1. Seismic model comparisons and crustal thickness

The 3D corrected ACCP model highlights the discontinuity structure of the forearc to arc (Fig. 5B–D), and all depths in the model are relative to sea level. The main features include: 1) a strong, positive east-dipping arrival along the majority of the margin starting at about 20 km depth near the coast and extending to the base of the model, 2) a generally weak positive arrival between the forearc high topography and the volcanic arc, and 3) a relatively shallow (~30–35 km depth), strong, positive arrival beneath the arc and backarc region. These arrivals generally correspond to estimates of crustal thickness derived from the shear-wave velocity model and the position of the downgoing oceanic lithosphere based on the model of McCrory et al. (2012). Using a combination of the corrected slab model, the crustal thickness model, and the ACCP images, we can also delineate the location of the forearc-mantle corner (FMC; i.e., where the crust of the overriding and downgoing plate separate) (Fig. 5A).

Trenchward of the FMC, overriding crustal thickness variations depend on the depth to the top of the slab, which is based on results of previous seismic studies (McCrory et al., 2012) and validated by the locations of low frequency earthquakes. The base of the overriding crust generally extends to depths between 20 and 30 km near the coastline, gradually increasing toward the FMC along the entire margin. The northern and southern portions of the margin appear to show slightly thinner forearc crust due to

the relatively shallower dip of the slab in these areas, while the base of the Siletzia terrane in central Cascadia forearc trenchward of the FMC is at ~30–35 km depth, consistent with wide-angle reflection and refraction results and shear-wave velocities that indicate Siletzia crustal material extends down to the plate interface (Delph et al., 2018; Trehu et al., 1994). In this region, a high amplitude positive arrival is observed at <10 km below the base of the forearc crust beginning at ~20 km depth near the coastline, and likely represents the Moho of the downgoing oceanic lithosphere. An exception to this can be seen in the northern portion of the study area, where this positive arrival overlaps with the estimated base of the crust, which is equivalent to the top of the oceanic slab (Fig. 5B). This may indicate that the velocity model used for migration is either too slow or has too high a Vp/Vs ratio to appropriately locate this arrival, as LFE locations are in agreement with the plate interface model. A Vp/Vs ratio of <1.7 would be needed to place this arrival at the expected depths given the shear-wave velocity structure of the margin from the joint inversion (Fig. S2), which is unlikely given the evidence for fluids in the crust. Therefore, a possible explanation for this disagreement is that we are sampling the slow axis of symmetry in an anisotropic material, as Rayleigh waves are fundamentally sensitive to only the vertical component of shear-wave velocity. This would be expected if this material is composed of near-horizontally foliated underplated material, as inferred in previous studies (e.g., Calvert et al., 2011; Delph et al., 2018). Elsewhere along the margin, this east dipping positive arrival is generally slightly deeper than the expected position for the top of the adjusted slab model, consistent with the Moho of the downgoing oceanic lithosphere.

Forearc crustal thickness estimates appear greatest at the FMC (Fig. 5A). To understand variations in the depth to the base of the crust under different geologic domains in the region, values are again presented relative to sea level. The depth to the forearc mantle corner (FMC) is on average 43.9 ± 3.9 km. Other stud-

ies have observed this apparent thickening of the crust along the Cascadia forearc, particularly in Washington, using various seismic techniques (Calvert et al., 2006; Preston et al., 2003; Ramachandran et al., 2006; Stanley et al., 1999). In the forearc between the FMC and the magmatic arc, crustal thickness is difficult to constrain, as arrivals that could be associated with the Moho become difficult to track. Relatively low amplitude arrivals at depths ~ 40 km can sometimes be observed and traced throughout the forearc (Fig. 5C), however it is more common to see a rather disjointed zone of weak arrivals consistent with a very low velocity contrast at these depths, in agreement with the shear-wave velocity model. In areas where an arrival that could be interpreted as the Moho was apparent, we manually modified the crustal thickness model based on these images, but the consistency between the interpreted Moho arrival and the 4.2 km/s contour in the shear-wave velocity model led to only small changes in the final crustal thickness model.

In the eastern portion of the study area, a clear, high amplitude arrival at 30–40 km depth can be tracked throughout arc and backarc. This arrival corresponds to the depths at which the Vs model reaches >4.2 km/s, consistent with the Moho. Moho depth beneath the Cascadia volcanic arc (red triangles; Fig. 5A) is on average 37.6 ± 3.6 km. However, within the arc, Moho depth variations show a bimodal distribution, with greater depths (44.4 ± 2.7 km) observed from 45.8° – 48°N beneath the edifices and fields that include Indian Heaven, St. Helens, Adams, and Rainier, and shallower depths beneath the arc to the north and south (36.2 ± 1.6 km). This thinning trend from the FMC toward the arc can be clearly observed in the ACCP and Vs models for profiles perpendicular to the margin (Fig. 5B–G, black dashed line above topography).

3.2. Average forearc shear-wave velocities

Using the crustal thickness surface we created, we can estimate the average properties of different portions of the model to gain insight into general shear-wave velocity characteristics along the Cascadia margin. For the crust, we calculate the average velocity above the crustal thickness model presented in Fig. 2A, whereas for the forearc mantle, we calculate the average velocity of up to 20 km below the crustal thickness estimate depending on whether the slab limits the thickness of the mantle wedge. Of course, uncertainties in the depth to the base of the crust will be reflected in these values. Thus, small-scale features (only a few model grid points, or $<0.3^\circ$) in the resulting maps should be interpreted with caution, however average properties over large spatial scales are likely robust.

Average crustal shear-wave velocities in the overriding plate along the Cascadia margin correlate well with results from previous studies. Within the forearc, velocities in the crust largely reflect the geology at the surface. Fast velocities are clearly associated with the Siletzia terrane (blue polygon, Fig. 6A), and although small regions of slightly lower velocities underlie this terrane (~ 3.4 km/s; Fig. 5F), the much faster velocities of the Siletzia terrane dominate the average Vs structure. Beneath the northern Cascadia margin, the low average Vs is largely related to the Olympic Accretionary Complex and its associated lower crustal LVZ (Figs. 5E, 6A). In the south, the lower average Vs is associated with the more silicic compositions of the Klamath terrane in combination with the lower crustal LVZ that mirrors the structure seen along the northern Cascadia margin (Fig. 5G). These variations in forearc crustal structure were observed and interpreted by Delph et al. (2018). In the forearc mantle wedge of Cascadia, we find that Vs is significantly slower than expected for uppermost mantle (~ 4.0 km/s; Fig. 6B). The uppermost mantle, which is composed dominantly of peridotite, should have a Vs of ~ 4.47 km/s based on global models (Kennett and Engdahl, 1991). This observation

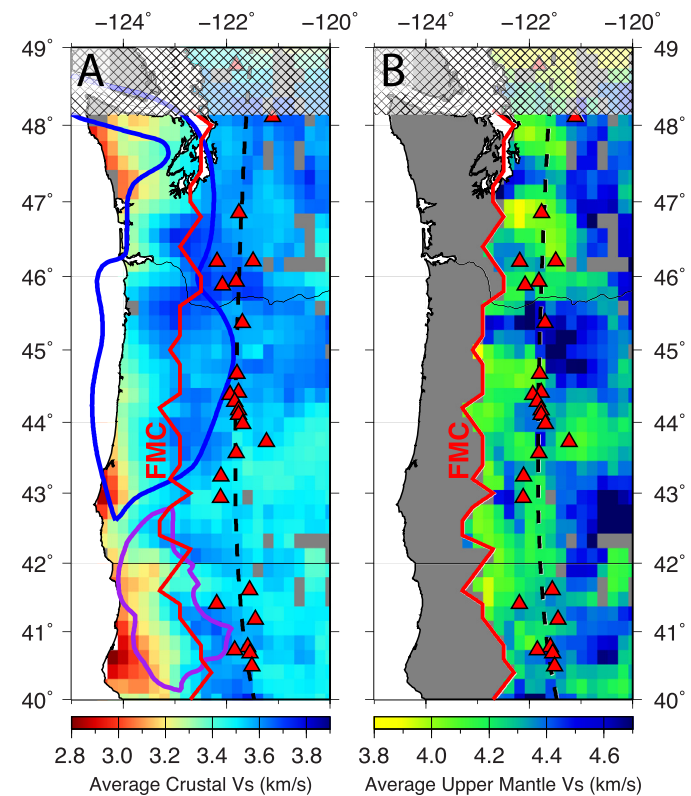


Fig. 6. Average shear-wave velocity along the Cascadia margin. Dashed line: modern arc axis; red triangles, Holocene volcanic centers; red line, forearc mantle corner (FMC) (A) Cascadia crust: low velocities (<3.4 km/s) are observed along the northern and southern Cascadia margin, corresponding surficially to the Olympic Accretionary Complex (north; indent along western boundary of Siletzia terrane) and Klamath terrane (south; purple polygon). The Siletzia terrane (blue polygon) is characterized by high shear-wave velocities throughout most of the forearc. (B) Uppermost mantle: average shear-wave velocities are slow in the forearc mantle wedge (west of dashed line) compared to the foreland mantle wedge (east of dashed line), likely due to pervasive serpentinization. Blue colors correspond to shear velocities expected for typical uppermost mantle.

is consistent with previous studies that suggest pervasive serpentinization beneath the Cascadia forearc mantle wedge on a regional scale (e.g., Brocher et al., 2003; Abers et al., 2017).

4. Discussion

4.1. Forearc subcretion

The thickest overriding plate crust is generally found near the forearc mantle corner along the Cascadia margin, reaching up to ~ 50 km and thinning in both the seaward and landward directions (Fig. 5A). This observation is consistent with the findings of smaller-scale studies (Ramachandran et al., 2006; Preston et al., 2003; Stanley et al., 1999; Calvert et al., 2006), and has been explained by basal accretion and structural duplexing within crustal material near the base of the overriding plate (Calvert et al., 2006). In this process, which we refer to as “subcretion”, slices of either the overriding or downgoing plate detach, are transported deeper into the subduction zone, and accrete to the base of the overriding plate due to strength variations in the overriding plate's crust, the frictional properties of the plate interface, or the subcreted packages relatively low density compared to mantle wedge material.

In Cascadia, this subcreted material may be dominantly composed of sedimentary material. In northern Cascadia, a highly reflective zone that thickens arcward to >10 km is interpreted as underplating sediments, perhaps with some intercalated basaltic slivers, and extends to ~ 40 – 50 km depth (the “E” reflectors; Calvert

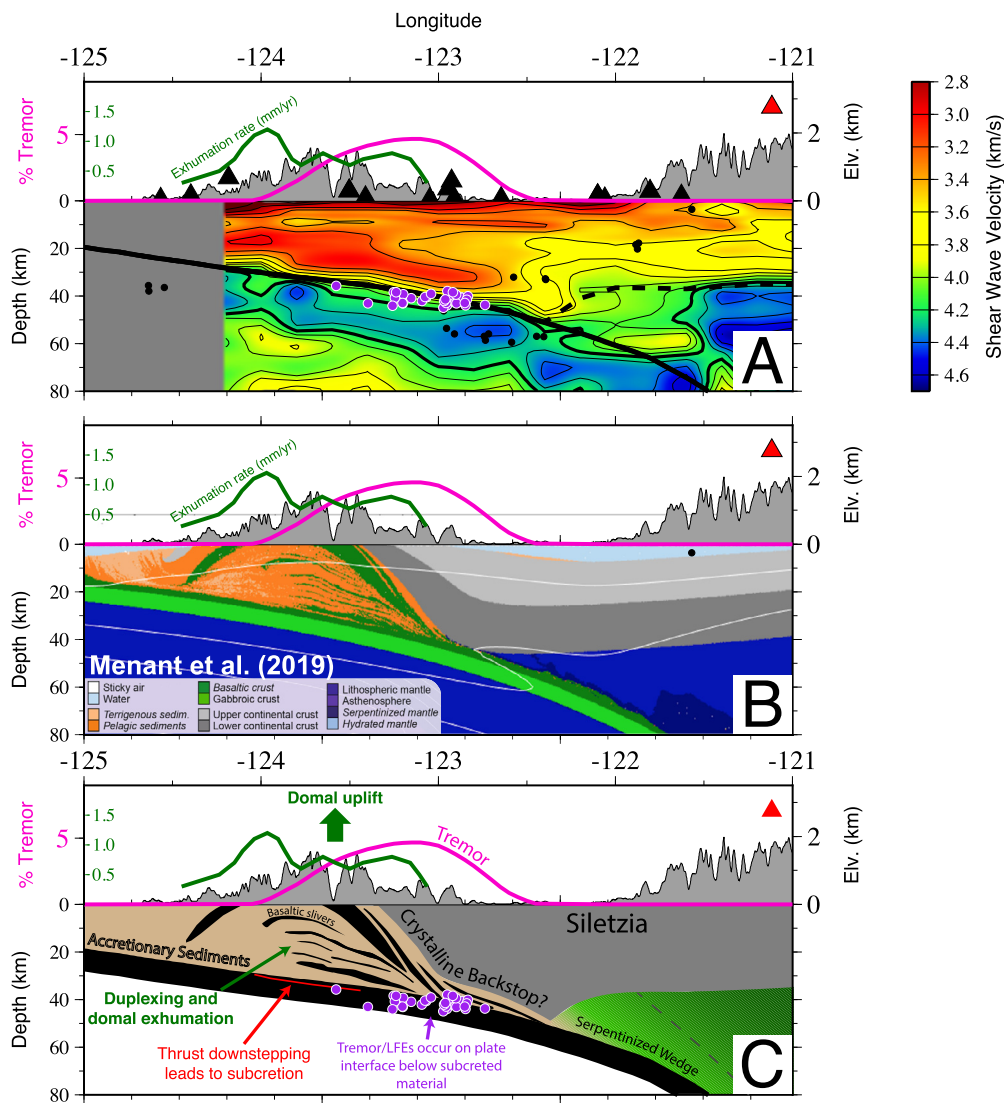


Fig. 7. Cross-section of presumed structure beneath the Olympic accretionary complex (Lat: 48.0°N). (A) Shear-wave velocity model (Delph et al., 2018). LVZ parallels downgoing slab (solid black line; McCrory et al., 2012), is underlain by LFEs (purple dots, Royer and Bostock, 2014), and spatially correlates with non-volcanic tremor (fuchsia line on topography). Green line shows exhumation rates in the Olympic Mountains from apatite fission-track dating (Brandon et al., 1998), which correlates with LVZ location. Dashed black line: Moho depth from this study; Black dots: earthquakes; red triangle, Rainier volcano projected onto cross section. (B) Thermomechanical model modified from Menant et al. (2019) and scaled to align inferred structure with velocity model. Dark green represents basaltic shivers of the upper oceanic crust, orange represents sedimentary material. (C) Simplified conceptual cartoon combining seismic velocity model with implications from thermomechanical model.

et al., 2011; Clowes et al., 1987; Nedimović et al., 2003). This zone is also characterized by strong P- and S-wave velocity reductions (Vs as low as 2.8 km/s, Calkins et al., 2011; Calvert et al., 2011; Delph et al., 2018; Ramachandran et al., 2006). The subduction décollement itself is interpreted as lying at or near the base of this highly reflective low velocity zone (LVZ), consistent with low frequency earthquake hypocenters (Figs. 5E, 7A; Calvert et al., 2020). Both the top of intraslab seismicity in the Juan de Fuca plate and a deeper reflection signal interpreted as the downgoing plate Moho reflection (PmP) are > 8 km below the base of the E reflections (Calvert et al., 2006). This LVZ has been previously interpreted as fluids within oceanic crust below a sealed interface (Audet et al., 2010, 2009) although if this interpretation is correct, the presence of low frequency earthquakes below this LVZ would require these seismic events to occur well within the downgoing plate's crust (Fig. 5E; Audet and Schaeffer, 2018). Rather, in light of: 1) the low frequency earthquake hypocenters, 2) the thickness of the LVZs, 3) the very low velocities within the LVZs, 4) high reflectivity features within the LVZs, 5) the timing of the PmP arrival from the downgoing plate, and 6) the correlation with relative Bouguer gravity

lows (Fig. 1), we find the interpretation that these LVZs dominantly comprise subcreted sedimentary material to be more compelling than oceanic crust, at least along the northern and southern portions of the Cascadia forearc (Fig. 7). This does not imply that the material doesn't contain any subcreted oceanic crustal material, but rather the proportions of oceanic crust within the material is similar to what is seen in exhumed subduction melanges, which are predominantly matrix supported (Bebout and Penniston-Dorland, 2016; Grigull et al., 2012). The proportion of subcreted oceanic crust to sedimentary material may vary along the margin, as P-wave velocities further north show a similar LVZ in spatial extent but appear faster than would be expected from underplating sediments, and thus may comprise dominantly oceanic mafic lithologies (Calvert et al., 2020). This may also be the case in central Cascadia, as the crust still appears thickest near the mantle wedge, but there is no associated significant LVZ.

A similar LVZ to that seen beneath northern Cascadia is observed within the lower crust of the overriding plate in southern Cascadia (Fig. 5G) (Delph et al., 2018; Liu et al., 2012). This LVZ is also characterized by high reflectivity from controlled-source imag-

ing in a number of studies (Beaudoin et al., 1998, 1996; Fuis et al., 1987), although it is not as clearly imaged. At shallower depths, the LVZ has been interpreted as oceanic and sedimentary material from a subunit of the Klamath terrane (Fuis et al., 1987) or as underthrust Franciscan accretionary material (Beaudoin et al., 1998, 1996). At greater depths, where it consists of slightly higher (but still low) shear-wave velocities, it has been interpreted as either underplated, fluid-filled Franciscan material (Delph et al., 2018) or serpentinized mantle (Liu et al., 2012), although it is likely too slow to consist of the latter (3.6–3.8 km/s vs. an expected Vs of ~4.0 km/s for serpentinized peridotite). This LVZ appears to connect at shallow depths to exposed Franciscan rocks (e.g., Beaudoin et al., 1996; Delph et al., 2018) and thus may relate to the areal extent of the underthrust Franciscan terrane. However, the low velocities are slower than expected for dry Franciscan terrane lithologies, implying that this material is infiltrated by fluids derived from modern subduction dehydration. Also, plate locking models have difficulty fitting observed uplift rates in the southern Cascadia forearc (e.g., Schmalzle et al., 2014) perhaps indicating that subcretion is ongoing.

The subcretion of sedimentary material can contribute to uplift and/or high exhumation rates and the building of topography in both isostatic and dynamic ways: 1) it will generally decrease the bulk density of the crust, as well as thicken the crust near the forearc-mantle corner of the overriding plate, resulting in an isostatic adjustment, and 2) it can dynamically lift overlying crustal material as it detaches from the downgoing plate (Litchfield et al., 2007; Menant et al., 2020). This dynamic process also results in broad, domal uplift and exhumation of the overriding crust based on these models, providing a predictive pattern that can be independently investigated in the field as evidence for this process. In northern Cascadia, the Olympic Mountains show a striking domal uplift and exhumation pattern based on low-temperature thermochronology (e.g., Brandon et al., 1998), which is spatially coincident with our LVZ (Fig. 7). While the Olympic accretionary complex doesn't extend to the surface along the entire margin, the LVZ we image appears to extend farther northward beneath Vancouver Island (Savard et al., 2018), indicating that this underplating process is occurring along a broad portion of the northern Cascadia margin. Interestingly, relative sea level has dropped ~1–2 m in the last 3000 yrs based on variations in sediments and microfossils at a coastal lake on Vancouver Island, compared to a relative rise in sea level of ~2–3 m over the same time period in central Cascadia where thick LVZs are not observed (Hutchinson et al., 2000). This time range represents multiple seismic cycles and indicates anelastic processes along the margin that would be consistent with subcretion and differential topographic development.

Sedimentary underplating has been invoked in the forearcs of other warm subduction zones to explain high topography, uplift, and exhumation rates as well, such beneath the Raukumara Range in northern New Zealand (Litchfield et al., 2007; Sutherland et al., 2009), the Chugach Mountains along southeastern Alaska (Arkle et al., 2013), and in the central Chilean forearc (Muñoz-Montecinos et al., 2020; Saillard et al., 2009). Along these margins, the underplating of material corresponds to high topography, high uplift rates, and exhumation in the overriding plate. This is further supported by seismic images that show very similar forearc structures to what we present here (e.g., Chile, Comte et al., 2019; Chugach, Ward and Lin, 2018; Raukumara, Reyners et al., 2006). This process can also create a positive feedback, whereby higher topography leads to higher erosion rates, and thus more recycling of sediment back into the trench. However, seismic reflection and refraction images near the Juan de Fuca trench show the opposite of what one might predict given topography variations along the margin, indicating that a thicker wedge of sediments underthrusts beneath central Cascadia near the trench than further to the north (1.7 km

vs. <0.5 km; Han et al., 2017). It is important to note that these seismic images only extend to very shallow depths along the plate interface (~5 km below the seafloor) and thus may not be applicable to what is happening deeper in the subduction channel. For instance, the thick crust of the Siletzia terrane in the forearc of central Cascadia (~30 km) likely acts as a backstop to sediment subduction where it extends down to the plate interface and farther trenchward (approximately between 43° and 46° N; Trehu et al., 1994; Delph et al., 2018), which could inhibit the deep underplating of sedimentary material. In contrast, the Klamath terrane and the northern portion of the Siletzia terrane are much thinner (~15 km), perhaps allowing for the deeper transport and easier accommodation of sedimentary material. Regardless of the precise control on subcretion, these LVZs in the northern and southern Cascadia forearc highlight regions of increased exhumation and uplift, and likely represent areas that are currently experiencing lower crustal underplating of primarily sedimentary material, consistent with the Bouguer gravity signature of the forearc.

The presumed areas of sediment underplating also correlate with plate locking behavior along the margin (Li et al., 2018; Schmalzle et al., 2014). Drastic lateral variations in plate locking behavior have been modeled based on the combination of vertical and horizontal uplift data on land. It should be noted that this variation is less pronounced in locking models that primarily used horizontal GPS motions to model plate locking, but nonetheless still exists (e.g., McCaffrey et al., 2007; Li et al., 2018). Schmalzle et al. (2014) also notes that, despite the inclusion of vertical uplift data, their locking model still could not explain the uplift rates in northern California, which spatially correspond with the interpreted subcreted sedimentary material from our velocity model. This indicates that processes other than plate locking likely play a role in uplift rates and the resulting topography along the margin.

4.2. Linking lateral variations to seismic structure

Disentangling the contributions from variations in overriding plate characteristics from larger geodynamic controls has proven difficult. Many studies focus on a single characteristic, and then infer or interpret relationships with other margin characteristics based on those interpretations. For example, Brudzinski and Allen (2007) infer an overriding plate control on episodic tremor and slip due to the correlation with terrane boundaries at the surface. Overriding plate controls appear to be favored by studies that focus on shallower (i.e., crustal) characteristics such as faults or crustal shear-wave velocities (Delph et al., 2018; Wells et al., 2017). However, clear variations in the deeper structure of the margin (i.e., slab and subslab) are also observed (e.g., Bodmer et al., 2018, 2020) and have alternatively been proposed to be the primary control on variations in the manifestation of subduction along the margin. It is likely that both play a role in controlling margin variation. Here, we attempt to link contributions of individual observations into a conceptual model for the Cascadia subduction zone that satisfies all observations (summarized in Fig. 8).

The morphology of the subducting slab appears to exert a first order control on some of the features along the margin (Bostock et al., 2019). For instance, in both northern and southern Cascadia, the slab has higher along-strike and downdip curvature than in the central Cascadia, which correlates well with the distribution of intraslab seismicity (Fig. 8B,C; Bostock et al., 2019; Hayes et al., 2018; McCrory et al., 2012). This curvature in combination with slab pull results in tensional stresses at shallow depths within the subducting slab oriented in the down dip direction, consistent with stress orientations derived from focal mechanisms of intraslab seismicity (Wada et al., 2010). What controls this slab morphology, however, is less clear. Rollback-driven mantle flow around the retreating and relatively narrow Juan de Fuca slab could produce

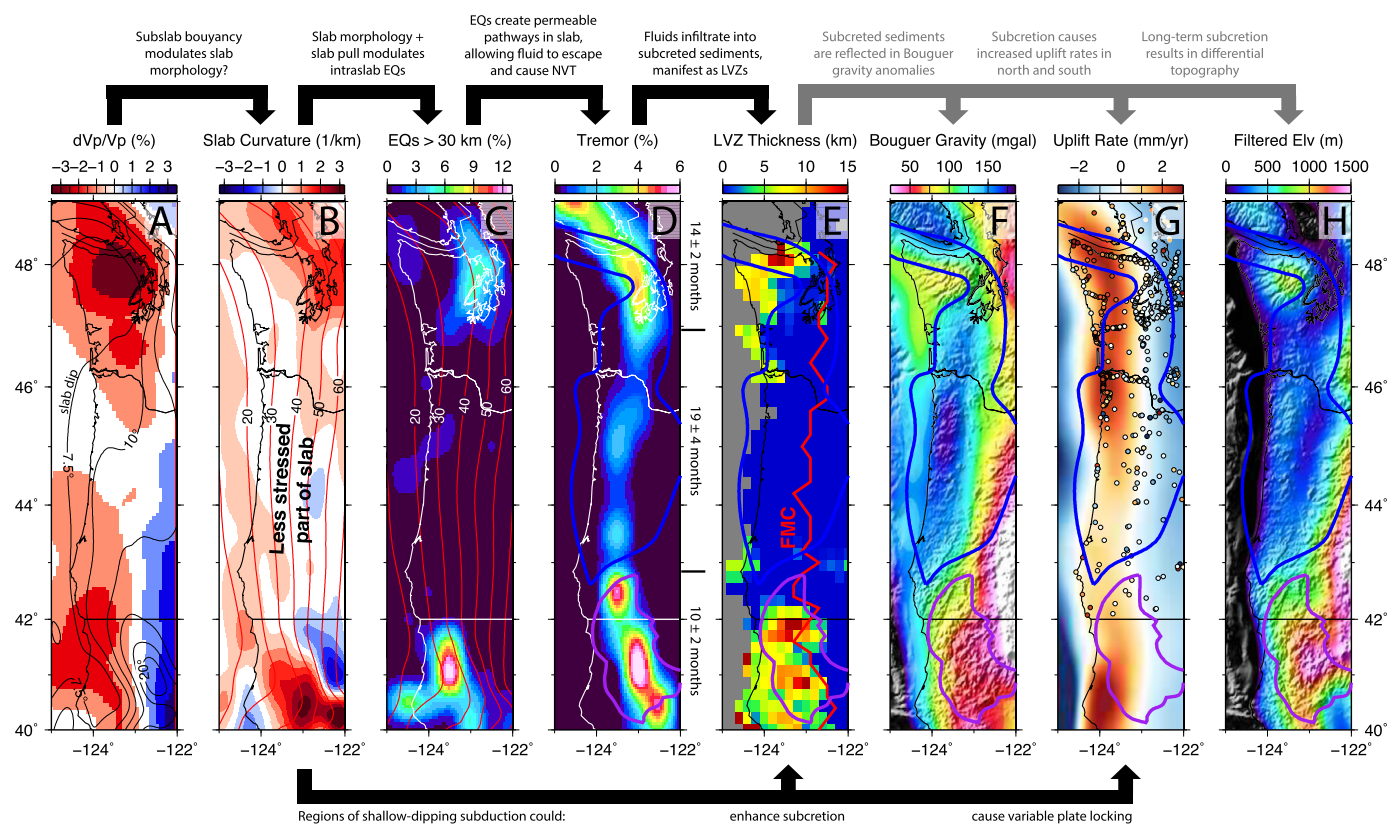


Fig. 8. Lateral variations along the Cascadia forearc. (A) Average upper mantle (sub-slab) P-wave velocities (from 100–250 km depth; Bodmer et al., 2018) and revised slab surface dip angle (from Fig. 4A; contours every 2.5°). (B) Revised slab surface curvature from principal curvature analysis. Red highlights regions of slab convexity and blue highlights regions of concavity (relative to overriding plate, respectively). Red contours are slab depth from the revised slab model. Stress inference from Wada et al. (2010). (C) Seismicity > 30 km, most of which occurs within the downgoing slab (USGS NEIC catalog). Red contours same as in (B). (D) Non-volcanic tremor density (Wech, 2010) and slow slip recurrence intervals (Brudzinski and Allen, 2007). (E) LVZ thicknesses used as a proxy for subcreted sedimentary packages (Delph et al., 2018). Thickness defined by $V_s < 3.2 \text{ km/s}$ at >10 km depth. FMC (red line): forearc mantle corner. (F) Gaussian-filtered Bouguer gravity anomaly with a 1σ of 25 km. Low Bouguer gravity anomalies in the forearc are consistent with low density material in the crust. (G) Predicted interseismic uplift rates from the locking model of Li et al. (2018). Circles are decadal uplift rates from GPS and tide gauges. (H) Gaussian-filtered elevation with a 1σ of 25 km. Blue polygon: Siletzia Terrane. Purple polygon: Klamath terrane.

the first order observed morphology (e.g., Schellart et al., 2007), but whether mantle shear-wave splitting supports this flow pattern is debated (Zandt and Humphrey, 2008; Bodmer et al., 2015). Alternatively, recent tomographic images show low velocity zones below the Juan de Fuca slab, which are interpreted as regions of buoyancy and correlate with shallow slab dip angles (Fig. 8A; Bodmer et al., 2020). In this case, the westward migration of the Cascadia trench combined with subslab buoyancy could impede slab rollback and lead to a shallower angle of subduction above these buoyancy anomalies (e.g., Schepers et al., 2017). Regardless of the specific mechanism, the higher convex curvature of the Juan de Fuca slab surface relative to the overriding plate appears to increase differential stress and lead to elevated rates of intraslab seismicity along the northern and southern portion of the margin.

Higher rates of intraslab seismicity likely reflect regions of increased deformation, and therefore permeability, in the downgoing plate. This increased permeability may allow for fluids sourced from dehydration reactions to migrate to shallower depths more readily and contribute to the NVT distribution along the margin. As discussed in detail in Delph et al. (2018), it is unlikely that variations in hydration within the downgoing slab controls NVT distribution, as offshore seismic studies appear to show either no clear correlation or an anticorrelation between NVT and proxies for crustal and upper mantle hydration in the Juan de Fuca plate prior to subduction, such as seismic velocities, seismicity, and the depth of fault penetration into the oceanic lithosphere (e.g., Han et al., 2016, 2018; Canales et al., 2017; Stone et al., 2018; VanderBeek and Toomey, 2019). Margin thermal structure is also unlikely

to contribute to the along-strike distribution of NVT, as variations in the thermal structure along this portion of Cascadia are too small to lead to significant differences in the depth of slab dehydration (Condit et al., 2020). Therefore, it is likely that regions of high intraslab seismicity indicate increased permeability within the subducting lithosphere, which allows for fluid egress into the interplate boundary and causes higher amounts of NVT.

Regions with a high density of NVT and more frequent slow slip events also correlate with low phase and shear-wave velocities in the Cascadia forearc (Figs. 7, 8D,E; Porritt et al., 2011; Delph et al., 2018; Janiszewski et al., 2019) inferred to represent regions of subcreted sedimentary material. However, the connection between tremor, slow slip, and subcretion remains somewhat unclear. Low-frequency earthquakes and tremor are thought to occur in regions of elevated pore fluid pressure as evidenced by their sensitivity to small magnitude stress changes (e.g. Royer et al. 2015) and occurrence in regions of elevated V_p/V_s ratios. Previous authors have argued that the plate boundary itself acts as a permeability barrier owing to processes such as mineralization and shear-induced grain size reduction (e.g. Bostock et al., 2019), which promotes the development of fluid overpressure. The process of subcretion could further contribute to this impermeability, as it likely involves downstepping of the active shear zone, which leads to the successive emplacement of slices of material from the downgoing plate to the overriding plate (Fig. 7; Menant et al., 2019). Hence, in regions of active subcretion, a zone of vertically-impermeable, low-angle relict shear zones may lie atop the active plate boundary, further decreasing permeability and promoting high fluid pressure and the

resulting higher density of NVT. While this mechanism is appealing, geodynamic models of subcretion appear to be driven by a transition to higher strength along the plate boundary, which is difficult to reconcile with evidence for a mechanically weak plate boundary at these locations. One possibility is that the high friction of the seismogenic portion of the plate interface (*updip* of the slow slip zone) drives subcretion by promoting higher shear strength and positive shear strength gradients along the subduction interface (e.g., Menant et al., 2019). In this case, the shear strength of the interface could be controlled by its rheological properties or a shallow angle of subduction, and would lead to the transfer of slices from the downgoing plate to the overriding plate as the plate interface attempts to adjust to a more energetically favorable state. This is consistent with the correlation between regions of higher coupling along the plate interface as reflected in modeled interseismic uplift rates (Fig. 8G; Schmalzle et al., 2014; Li et al., 2018), slab dip and curvature (Fig. 8A,B), and inferred subcretion, and has also been interpreted elsewhere along the margin (e.g., Calvert et al., 2006). Alternatively (or in addition), fluid-mediated weakening of material near the plate interface could allow it to transfer easily to the base of the overriding plate, and backstop rheology and geometry, which clearly varies along the margin (e.g., Trehu et al., 1994) could control the amount of subcreted material that can be accommodated at lower crustal depths.

As discussed in Section 4.1, the process of subcretion is a first-order control on variations in uplift rates, erosion rates, and associated topography in Cascadia. Bodmer et al. (2020) proposed an alternative hypothesis to explain these geologically-observable variations in which subslab buoyancy anomalies control slab dip, and thereby modulate the effective friction along the plate interface as expressed in plate locking behavior (Fig. 8A,G; Li et al., 2018; Schmalzle et al., 2014). This would lead to differential topographic development over geologic time as long as there is an anelastic component of deformation (i.e., deformation that is not recovered during the seismic cycle). Subcretion could represent this anelastic deformation if unfavorable interface geometry or variable interface locking is the dominant control on subcretion. However, this mechanism neglects the likely contributions of significant variations in overriding plate composition and architecture. Further studies on the subslab structure of other forearcs displaying similar variations (e.g., Scholl, 2019; Menant et al., 2020) are necessary to determine whether these buoyancy anomalies are a fundamental control on subcretion and the surface expression of subduction.

In conclusion, lateral variations in the manifestation of subduction along the Cascadia margin appear to have interrelated mechanisms, but their interplay is by no means simple. Changes in the geometry of the plate interface lead to variations in plate locking, and the contortion of the subducting slab leads to intraslab seismicity. This seismicity creates permeable pathways for fluids to escape from the downgoing plate and cause variable NVT density and slow slip recurrence intervals along the margin. In addition, frictional variations due to the geometry of the plate interface, the pre-existing architecture/strength of the overriding plate, and/or fluid-mediated weakening of material near the plate interface leads to variations in subcretion. This in turn controls long-term variations in uplift, and therefore topographic development along the Cascadia forearc, and may further contribute to heterogeneous distributions of NVT.

5. Conclusion

Significant lateral variations in seismicity and other geophysical observations along the Cascadia forearc cannot be explained by variations in only the overriding or downgoing plate. To better understand how these variations are linked to the seismic structure

of the margin, we applied a 3D variable Vp/Vs ratio velocity model correction to P-wave radial receiver functions to create a model of discontinuity structure for the Cascadia margin. When interpreted alongside a recently published shear-wave velocity model (Delph et al., 2018), our results highlight regions crustal thickening due to the successive emplacement and transfer of material from the downgoing to overriding plate ("subcretion"). Along the northern and southern portion of the margin, this subcreted material corresponds to thick low shear-wave velocity zones with high internal reflectivity and correlates with relatively low Bouguer gravity signatures in the forearc. These factors indicate that these zones comprise dominantly (meta)sedimentary material. In addition, the spatial association of this subcreted material with high non-volcanic tremor and short slow slip recurrence intervals indicates that fluids are prevalent in these regions. The inherent vertical impermeability of these subcreted packages may accentuate this correlation, however variations in the permeability of the downgoing slab as inferred from its stress state and intraslab seismicity distribution are likely the first-order control on variations in fluid-mediated processes. Lastly, variations in the amount of subcretion appear related to changes in plate interface geometry/rheology, likely alongside overriding plate architecture, and ultimately controls variable exhumation and uplift rates along the Cascadia margin and the resulting forearc topography over geologic timescales.

CRediT authorship contribution statement

Jonathan R. Delph: Conceptualization, Investigation, Methodology, Visualization, Writing – original draft, Writing – review & editing. **Amanda M. Thomas:** Funding acquisition, Investigation, Methodology, Supervision, Writing – review & editing. **Alan Levander:** Writing – review & editing.

Declaration of competing interest

The authors declare that they have no known competing financial interests or personal relationships that influenced this research.

Acknowledgements

This research was funded by NSF #1848302. This manuscript benefitted from constructive reviews by Andrew Calvert and Rob Porritt as well as an informal review by Doug Toomey. The authors want to thank Tyler Newton for sharing tide gauge and GPS decadal uplift rate measurements, Miles Bodmer for sharing his tomographic model, Armel Menant for sharing his thermomechanical model, Shaoyang Li and Gina Schmalzle for the locking model predictions, and Michael Bostock and Alexandre Plourde for LFE P and S travel times and locations. Earthquake P and S travel times were accessed through the Northern California Earthquake Data Center (NCEDC; doi: <https://doi.org/10.7932/NCEDC>) using the comcat Python library (<https://doi.org/10.5066/P91WN1UQ>). Statements and interpretations based on the shared data and data products presented in this paper belong to the authors and do not necessarily represent the ideas of the aforementioned contributors. The facilities of IRIS Data Services, and specifically the IRIS Data Management Center, were used for access to waveforms, related metadata, and/or derived products used in this study. IRIS Data Services are funded through the Seismological Facilities for the Advancement of Geoscience (SAGE) Award of the National Science Foundation under Cooperative Support Agreement EAR-1851048.

Appendix A. Supplementary material

Supplementary material related to this article can be found online at <https://doi.org/10.1016/j.epsl.2020.116724>.

References

- Abers, G.A., Van Keeken, P.E., Hacker, B.R., 2017. The cold and relatively dry nature of mantle forearcs in subduction zones. *Nat. Geosci.* 10, 333–337. <https://doi.org/10.1038/ngeo2922>.
- Arkle, J.C., Armstrong, P.A., Haeussler, P.J., Prior, M.G., Hartman, S., Sendziak, K.L., Brush, J.A., 2013. Focused exhumation in the syntaxis of the western chugach mountains and prince William sound, Alaska. *Bull. Geol. Soc. Am.* 125, 776–793. <https://doi.org/10.1130/B30738.1>.
- Audet, P., Schaeffer, A.J., 2018. Fluid pressure and shear zone development over the locked to slow slip region in Cascadia. *Sci. Adv.* 4, eaar2982. <https://doi.org/10.1126/sciadv.aar2982>.
- Audet, P., Bostock, M.G., Christensen, N.I., Peacock, S.M., 2009. Seismic evidence for overpressured subducted oceanic crust and megathrust fault sealing. *Nature* 457, 76–78. <https://doi.org/10.1038/nature07650>.
- Audet, P., Bostock, M.G., Boyarko, D.C., Brudzinski, M.R., Allen, R.M., 2010. Slab morphology in the Cascadia fore arc and its relation to episodic tremor and slip. *J. Geophys. Res., Solid Earth* 115, 1–15. <https://doi.org/10.1029/2008JB006053>.
- Balco, G., Finnegan, N., Gendaszek, A., Stone, J.O.H., Thompson, A., 2013. Erosional response to northward-propagating crustal thickening in the coastal ranges of the U.S. Pacific northwest. *Am. J. Sci.* 313, 790–806. <https://doi.org/10.2475/11.2013.01>.
- Beaudoin, B.C., Godfrey, N.J., Klemperer, S.L., Lendl, C., Trebu, A.M., Henstock, T.J., Levander, A., Holl, J.E., Meltzer, A.S., Luetgert, J.H., Mooney, W.D., 1996. Transition from slab to slabless: results from the 1993 Mendocino triple junction seismic experiment. *Geology* 24, 195–199. [https://doi.org/10.1130/0091-7613\(1996\)024<195:TFSTSR>2.3.CO;2](https://doi.org/10.1130/0091-7613(1996)024<195:TFSTSR>2.3.CO;2).
- Beaudoin, B.C., Hole, J.A., Klemperer, S.L., Tréhu, A.M., 1998. Location of the southern edge of the Gorda slab and evidence for an adjacent asthenospheric window: results from seismic profiling and gravity. *J. Geophys. Res., Solid Earth* 103, 30101–30115. <https://doi.org/10.1029/98JB02231>.
- Bebout, G.E., Penniston-Dorland, S.C., 2016. Fluid and mass transfer at subduction interfaces—the field metamorphic record. *Lithos* 240–243, 228–258. <https://doi.org/10.1016/j.lithos.2015.10.007>.
- Blakely, R.J., Brocher, T.M., Wells, R.E., 2005. Subduction-zone magnetic anomalies and implications for hydrated forearc mantle. *Geology* 33, 445. <https://doi.org/10.1130/G21447.1>.
- Bodmer, M., Toomey, D.R., Hooft, E.E., Nábelek, J., Braunmiller, J., 2015. Seismic anisotropy beneath the Juan de Fuca plate system: evidence for heterogeneous mantle flow. *Geology* 43, 1095–1098. <https://doi.org/10.1130/G37181.1>.
- Bodmer, M., Toomey, D.R., Hooft, E.E., Schmandt, B., 2018. Buoyant asthenosphere Beneath Cascadia influences megathrust segmentation. *Geophys. Res. Lett.*, 6954–6962. <https://doi.org/10.1029/2018GL078700>.
- Bodmer, M., Toomey, D.R., Roering, J.J., Karlstrom, L., 2020. Asthenospheric buoyancy and the origin of high-relief topography along the Cascadia forearc. *Earth Planet. Sci. Lett.* 531, 115965. <https://doi.org/10.1016/j.epsl.2019.115965>.
- Bostock, M.G., 2002. Kirchhoff-approximate inversion of teleseismic wavefields. *Geophys. J. Int.* 149, 787–795. <https://doi.org/10.1046/j.1365-246X.2002.01687.x>.
- Bostock, M.G., 2013. The Moho in subduction zones. *Tectonophysics* 609, 547–557. <https://doi.org/10.1016/j.tecto.2012.07.007>.
- Bostock, M.G., Christensen, N.I., Peacock, S.M., 2019. Seismicity in Cascadia. *Lithos* 332–333, 55–66. <https://doi.org/10.1016/j.lithos.2019.02.019>.
- Brandon, M.T., Roden-Tice, M.K., Carver, J.I., 1998. Late Cenozoic exhumation of the Cascadia accretionary wedge in the Olympic Mountains, northwest Washington state. *Bull. Geol. Soc. Am.* 110, 985–1009. [https://doi.org/10.1130/0016-7606\(1998\)110<985:LCAEOTC>2.3.CO;2](https://doi.org/10.1130/0016-7606(1998)110<985:LCAEOTC>2.3.CO;2).
- Brocher, T.M., Parsons, T., Trebu, A.M., Snelson, C.M., Fisher, M.A., 2003. Seismic evidence for widespread serpentinized forearc upper mantle along the Cascadia margin. *Geology* 31, 267–270.
- Brudzinski, M.R., Allen, R.M., 2007. Segmentation in episodic tremor and slip all along Cascadia. *Geology* 35, 907–910. <https://doi.org/10.1130/G23740A.1>.
- Burgette, R.J., Weldon, R.J., Schmidt, D.A., 2009. Interseismic uplift rates for western Oregon and along-strike variation in locking on the Cascadia subduction zone. *J. Geophys. Res., Solid Earth* 114, B01408. <https://doi.org/10.1029/2008JB005679>.
- Calkins, J.A., Abers, G.A., Ekstrom, G., Creager, K.C., Rondenay, S., 2011. Shallow structure of the Cascadia subduction zone beneath western Washington from spectral ambient noise correlation. *J. Geophys. Res., Solid Earth* 116, 1–20. <https://doi.org/10.1029/2010JB007657>.
- Calvert, A.J., Ramachandran, K., Kao, H., Fisher, M.A., 2006. Local thickening of the Cascadia forearc crust and the origin of seismic reflectors in the uppermost mantle. *Tectonophysics* 420, 175–188. <https://doi.org/10.1016/j.tecto.2006.01.021>.
- Calvert, A.J., Preston, L.A., Farahbod, A.M., 2011. Sedimentary underplating at the Cascadia mantle-wedge corner revealed by seismic imaging. *Nat. Geosci.* 4, 545–548. <https://doi.org/10.1038/ngeo1195>.
- Calvert, A.J., Bostock, M.G., Savard, G., Unsworth, M.J., 2020. Cascadia low frequency earthquakes at the base of an overpressured subduction shear zone. *Nat. Commun.* 11, 3874. <https://doi.org/10.1038/s41467-020-17609-3>.
- Canales, J.P., Carbotte, S.M., Nedimović, M.R., Carton, H., 2017. Dry Juan de Fuca slab revealed by quantification of water entering Cascadia subduction zone. *Nat. Geosci.* 10, 864–870. <https://doi.org/10.1038/ngeo3050>.
- Christensen, N.I., 1996. Poisson's ratio and crustal seismology. *J. Geophys. Res.* 101, 3139. <https://doi.org/10.1029/95JB03446>.
- Christensen, N.I., 2004. Serpentinites, peridotites, and seismology. *Int. Geol. Rev.* 46, 795–816. <https://doi.org/10.2747/0020-6814.46.9.795>.
- Clowes, R.M., Brandon, M.T., Green, A.G., Yorath, C.J., Brown, A.S., Kanasewich, E.R., Spencer, C., 1987. LITHOPROBE—southern Vancouver Island: Cenozoic subduction complex imaged by deep seismic reflections. *Can. J. Earth Sci.* 24, 31–51. <https://doi.org/10.1139/e87-004>.
- Comte, D., Farias, M., Roecker, S., Russo, R., 2019. The nature of the subduction wedge in an erosive margin: insights from the analysis of aftershocks of the 2015 Mw 8.3 Illapel earthquake beneath the Chilean Coastal Range. *Earth Planet. Sci. Lett.* 520, 50–62. <https://doi.org/10.1016/j.epsl.2019.05.033>.
- Condit, C.B., Guevara, V.E., Delph, J.R., French, M.E., 2020. Slab dehydration in warm subduction zones at depths of episodic slip and tremor. *Earth Planet. Sci. Lett.* 552, 116601. <https://doi.org/10.1016/j.epsl.2020.116601>.
- Creager, K., 2014. Collaborative Research: Illuminating the architecture of the greater Mount St. Helens magmatic systems from slab to surface. International Federation of Digital Seismograph Networks. https://doi.org/10.7949/SN/XD_2014.
- Crosbie, K.J., Abers, G.A., Mann, M.E., Janiszewski, H.A., Creager, K.C., Ulberg, C.W., Moran, S.C., 2019. Shear velocity structure from ambient noise and teleseismic surface wave tomography in the Cascades around Mount St. Helens. *J. Geophys. Res., Solid Earth* 2019JB017836. <https://doi.org/10.1029/2019JB017836>.
- Delph, J.R., Zandt, G., Beck, S.L., 2015. A new approach to obtaining a 3D shear wave velocity model of the crust and upper mantle: an application to eastern Turkey. *Tectonophysics* 665. <https://doi.org/10.1016/j.tecto.2015.09.031>.
- Delph, J.R., Ward, K.M., Zandt, G., Ducea, M.N., Beck, S.L., 2017. Imaging a magma plumbing system from MASH zone to magma reservoir. *Earth Planet. Sci. Lett.* 457, 313–324. <https://doi.org/10.1016/j.epsl.2016.10.008>.
- Delph, J.R., Levander, A., Niit, F., 2018. Fluid controls on the heterogeneous seismic characteristics of the Cascadia margin. *Geophys. Res. Lett.* 45, 11,021–11,029. <https://doi.org/10.1029/2018GL079518>.
- Dueker, K.G., Sheehan, A.F., 1997. Mantle discontinuity structure from midpoint stacks of converted P to S waves across the Yellowstone hotspot track. *J. Geophys. Res.* 102, 8313. <https://doi.org/10.1029/96JB03857>.
- Eagar, K.C., Fouch, M.J., James, D.E., 2010. Receiver function imaging of upper mantle complexity beneath the Pacific Northwest, United States. *Earth Planet. Sci. Lett.* 297, 141–153. <https://doi.org/10.1016/j.epsl.2010.06.015>.
- Fuis, G.S., Zucca, J.J., Mooney, W.D., Milkereit, B., 1987. Geologic interpretation of seismic-refraction results in Northeastern California. *Bull. Geol. Soc. Am.* 98, 53–65. [https://doi.org/10.1130/0016-7606\(1987\)98<53:AGIOSR>2.0.CO;2](https://doi.org/10.1130/0016-7606(1987)98<53:AGIOSR>2.0.CO;2).
- Grigull, S., Krohe, A., Moos, C., Wassmann, S., Stöckhert, B., 2012. "Order from chaos": a field-based estimate on bulk rheology of tectonic mélange formed in subduction zones. *Tectonophysics* 568–569, 86–101. <https://doi.org/10.1016/j.tecto.2011.11.004>.
- Han, S., Bangs, N.L., Carbotte, S.M., Saffer, D.M., Gibson, J.C., 2017. Links between sediment consolidation and Cascadia megathrust slip behaviour. *Nat. Geosci.* 10, 954–959. <https://doi.org/10.1038/s41561-017-0007-2>.
- Han, S., Carbotte, S.M., Canales, J.P., Nedimovic, M.R., Carton, H., 2018. Along-trench structural variations of the subducting Juan de Fuca Plate from multichannel seismic reflection imaging. *J. Geophys. Res., Solid Earth* 123, 3122–3146. <https://doi.org/10.1002/2017JB015059>.
- Han, S., Carbotte, S.M., Canales, J.P., Nedimovic, M.R., Carton, H., Gibson, J.C., Horning, G.W., 2016. Seismic reflection imaging of the Juan de Fuca plate from ridge to trench: new constraints on the distribution of faulting and evolution of the crust prior to subduction. *J. Geophys. Res., Solid Earth* 121, 1849–1872. <https://doi.org/10.1002/2015JB012416>.
- Hayes, G.P., Moore, G.L., Portner, D.E., Hearne, M., Flamme, H., Furtney, M., Smoczyk, G.M., 2018. Slab2, a comprehensive subduction zone geometry model. *Science* 362, 58–61. <https://doi.org/10.1126/science.aat4723>.
- Hutchinson, I., Guilbault, J.P., Clague, J.J., Bobrowsky, P.T., 2000. Tsunamis and tectonic deformation at the northern Cascadia margin: a 3000-year record from Deserted Lake, Vancouver Island, British Columbia, Canada. *Holocene* 10, 429–439. <https://doi.org/10.1191/09596830066654539>.
- Janiszewski, H.A., Gaherty, J.B., Abers, G.A., Gao, H., Eilon, Z.C., 2019. Amphibious surface-wave phase-velocity measurements of the Cascadia subduction zone. *Geophys. J. Int.* 217, 1929–1948. <https://doi.org/10.1093/gji/ggz051>.
- Julià, J., Ammon, C.J., Herrmann, R.B., Correig, A.M., 2000. Joint inversion of receiver function and surface wave dispersion observations. *Geophys. J. Int.* 143, 99–112. <https://doi.org/10.1046/j.1365-246x.2000.00217.x>.
- Kennett, B.L.N., Engdahl, E.R., 1991. Traveltimes for global earthquake location and phase identification. *Geophys. J. Int.* 105, 429–465. <https://doi.org/10.1111/j.1365-246x.1991.tb06724.x>.
- Li, S., Wang, K., Wang, Y., Jiang, Y., Dosso, S.E., 2018. Geodetically inferred locking state of the Cascadia Megathrust based on a viscoelastic Earth model. *J. Geophys. Res., Solid Earth* 123, 8056–8072. <https://doi.org/10.1029/2018JB015620>.

- Ligorria, J.P., Ammon, C.J., 1999. Iterative deconvolution and receiver function estimation. *Bull. Seismol. Soc. Am.* 89, 1395–1400.
- Litchfield, N., Ellis, S., Berryman, K., Nicol, A., 2007. Insights into subduction-related uplift along the Hikurangi margin, New Zealand, using numerical modeling. *J. Geophys. Res., Earth Surf.* 112, 1–17. <https://doi.org/10.1029/2006JF000535>.
- Littel, G.F., Thomas, A.M., Baltay, A.S., 2018. Using tectonic tremor to constrain seismic wave attenuation in Cascadia. *Geophys. Res. Lett.*, 1–9. <https://doi.org/10.1029/2018GL079344>.
- Liu, K., Levander, A., Zhai, Y., Porritt, R.W., Allen, R.M., 2012. Asthenospheric flow and lithospheric evolution near the Mendocino triple junction. *Earth Planet. Sci. Lett.* 323–324, 60–71. <https://doi.org/10.1016/j.epsl.2012.01.020>.
- McCaffrey, R., Qamar, A.I., King, R.W., Wells, R., Khazaradze, G., Williams, C.A., Stevens, C.W., Vollick, J.J., Zwick, P.C., 2007. Fault locking, block rotation and crustal deformation in the Pacific Northwest. *Geophys. J. Int.* 169, 1315–1340. <https://doi.org/10.1111/j.1365-246X.2007.03371.x>.
- McCarthy, C., Takei, Y., Hiraga, T., 2011. Experimental study of attenuation and dispersion over a broad frequency range: 2. The universal scaling of polycrystalline materials. *J. Geophys. Res.* 116, B09207. <https://doi.org/10.1029/2011JB008384>.
- McCrory, P.A., Blair, J.L., Waldhauser, F., Oppenheimer, D.H., 2012. Juan de Fuca slab geometry and its relation to Wadati-Benioff zone seismicity. *J. Geophys. Res., Solid Earth* 117, 1–24. <https://doi.org/10.1029/2012JB009407>.
- Menant, A., Angiboust, S., Gerya, T., 2019. Stress-driven fluid flow controls long-term megathrust strength and deep accretionary dynamics. *Sci. Rep.* 9, 1–11. <https://doi.org/10.1038/s41598-019-46191-y>.
- Menant, A., Angiboust, S., Gerya, T., Lacassin, R., Simoes, M., Grandin, R., 2020. Transient stripping of subducting slabs controls periodic forearc uplift. *Nat. Commun.* 11, 1823. <https://doi.org/10.1038/s41467-020-15580-7>.
- Moran, S.C., Lees, J.M., Malone, S.D., 1999. P wave crustal velocity structure in the greater Mount Rainier area from local earthquake tomography. *J. Geophys. Res., Solid Earth* 104, 10775–10786. <https://doi.org/10.1029/1999JB900036>.
- Muñoz-Montecinos, J., Angiboust, S., Cambeses, A., García-Casco, A., 2020. Multiple veining in a paleo-accretionary wedge: the metamorphic rock record of prograde dehydration and transient high pore-fluid pressures along the subduction interface (western series, central Chile). *Geosphere* 16, 1–22. <https://doi.org/10.1130/GES02227.1>.
- Nedimović, M.R., Hyndman, R.D., Ramachandran, K., Spence, G.D., 2003. Reflection signature of seismic and aseismic slip on the northern Cascadia subduction interface. *Nature* 424, 416–420. <https://doi.org/10.1038/nature01840>.
- Plourde, A.P., Bostock, M.G., Audet, P., Thomas, A.M., 2015. Low-frequency earthquakes at the southern Cascadia margin. *Geophys. Res. Lett.* 42, 4849–4855. <https://doi.org/10.1020/2015GL064363>.
- Porritt, R.W., Allen, R.M., Boyarko, D.C., Brudzinski, M.R., 2011. Investigation of Cascadia segmentation with ambient noise tomography. *Earth Planet. Sci. Lett.* 309, 67–76. <https://doi.org/10.1016/j.epsl.2011.06.026>.
- Preston, L.A., Creager, K.C., Crosson, R.S., Brocher, T.M., Trehu, A.M., 2003. Intrastab earthquakes: dehydration of the Cascadia Slab. *Science* 302 (302), 1197–1200. <https://doi.org/10.1126/science.1090751>.
- Ramachandran, K., Hyndman, R.D., Brocher, T.M., 2006. Regional P wave velocity structure of the northern Cascadia subduction zone. *J. Geophys. Res.* 111, 1–15. <https://doi.org/10.1029/2005JB004108>.
- Reyners, M., Eberhart-Phillips, D., Stuart, G., Nishimura, Y., 2006. Imaging subduction from the trench to 300 km depth beneath the central North Island, New Zealand, with Vp and Vp/Vs. *Geophys. J. Int.* 165, 565–583. <https://doi.org/10.1111/j.1365-246X.2006.02897.x>.
- Royer, A.A., Bostock, M.G., 2014. A comparative study of low frequency earthquake templates in northern Cascadia. *Earth Planet. Sci. Lett.* 402, 247–256. <https://doi.org/10.1016/j.epsl.2013.08.040>.
- Saillard, M., Hall, S.R., Audin, L., Farber, D.L., Héral, G., Martinod, J., Regard, V., Finkel, R.C., Bondoux, F., 2009. Non-steady long-term uplift rates and Pleistocene marine terrace development along the Andean margin of Chile (31°S) inferred from 10Be dating. *Earth Planet. Sci. Lett.* 277, 50–63. <https://doi.org/10.1016/j.epsl.2008.09.039>.
- Savard, G., Bostock, M.G., Christensen, N.I., 2018. Seismicity, metamorphism, and fluid evolution across the Northern Cascadia fore arc. *Geochem. Geophys. Geosyst.*, 1–17. <https://doi.org/10.1029/2017GC007417>.
- Schellart, W.P., Freeman, J., Stegman, D.R., Moresi, L., May, D., 2007. Evolution and diversity of subduction zones controlled by slab width. *Nature* 446, 308–311. <https://doi.org/10.1038/nature05615>.
- Schepers, G., van Hinsbergen, D.J.J., Spakman, W., Kosters, M.E., Boschman, L.M., McQuarrie, N., 2017. South-American plate advance and forced Andean trench retreat as drivers for transient flat subduction episodes. *Nat. Commun.* 8, 15249. <https://doi.org/10.1038/ncomms15249>.
- Schmalzle, G.M., McCaffrey, R., Creager, K.C., 2014. Central Cascadia subduction zone creep. *Geochem. Geophys. Geosyst.* 15, 1515–1532. <https://doi.org/10.1029/2013GC005172>.
- Scholl, D.W., 2019. Seismic imaging evidence that forearc underplating built the accretionary rock record of coastal North and South America. *Geol. Mag.* <https://doi.org/10.1017/S0016756819000955>.
- Shelly, D.R., Beroza, G.C., Ide, S., 2007. Non-volcanic tremor and low-frequency earthquake swarms. *Nature* 446, 305–307. <https://doi.org/10.1038/nature05666>.
- Stanley, D., Villaseñor, A., Benz, H., 1999. Subduction zone and crustal dynamics of western Washington: a tectonic model for earthquake hazards evaluation. *USGS Open-File Rep.*, 99–311.
- Stone, I., Vidale, J.E., Han, S., Roland, E., 2018. Catalog of offshore seismicity in Cascadia: insights into the regional distribution of microseismicity and its relation to subduction processes. *J. Geophys. Res., Solid Earth* 123, 641–652. <https://doi.org/10.1002/2017JB014966>.
- Sutherland, R., Stagpoole, V., Uruski, C., Kennedy, C., Bassett, D., Henrys, S., Scherwath, M., Kopp, H., Field, B., Toulmin, S., Barker, D., Bannister, S., Davey, F., Stern, T., Flueh, E.R., 2009. Reactivation of tectonics, crustal underplating, and uplift after 60 Myr of passive subsidence, Raukumara Basin, Hikurangi-Kermadec fore arc, New Zealand: implications for global growth and recycling of continents. *Tectonics* 28, 1–23. <https://doi.org/10.1029/2008TC002356>.
- Trehu, A.M., Asudeh, I., Brocher, T.M., Luetgert, J.H., Mooney, W.D., Nabelek, J.L., Nakamura, Y., 1994. Crustal architecture of the Cascadia forearc. *Science* 260 (266), 237–243. <https://doi.org/10.1126/science.266.5183.237>.
- van Keken, P.E., Hacker, B.R., Syracuse, E.M., Abers, G.A., 2011. Subduction factory: 4. Depth - dependent flux of H2O from subducting slabs worldwide. *J. Geophys. Res.* 116. <https://doi.org/10.1029/2010JB007922>.
- VanderBeek, B.P., Toomey, D.R., 2019. Pn tomography of the Juan de fuca and gorda plates: implications for mantle deformation and hydration in the oceanic lithosphere. *J. Geophys. Res., Solid Earth* 124, 8565–8583. <https://doi.org/10.1029/2019JB017707>.
- Wada, I., Mazzotti, S., Wang, K., 2010. Intraslab stresses in the Cascadia subduction zone from inversion of earthquake focal mechanisms. *Bull. Seismol. Soc. Am.* 100, 2002–2013. <https://doi.org/10.1785/0120090349>.
- Ward, K.M., Lin, F., 2018. Lithospheric structure across the Alaskan cordillera from the joint inversion of surface waves and receiver functions. *J. Geophys. Res., Solid Earth* 123, 8780–8797. <https://doi.org/10.1029/2018JB015967>.
- Wech, A.G., 2010. Interactive tremor monitoring. *Seismol. Res. Lett.* 81, 664–669. <https://doi.org/10.1785/gssrl.81.4.664>.
- Wells, R., Bukry, D., Friedman, R., Pyle, D., Duncan, R., Haeussler, P., Wooden, J., 2014. Geologic history of Siletzia, a large igneous province in the Oregon and Washington coast range: correlation to the geomagnetic polarity time scale and implications for a long-lived Yellowstone hotspot. *Geosphere* 10, 692–719. <https://doi.org/10.1130/GES01018.1>.
- Wells, R.E., Blakely, R.J., Wech, A.G., McCrary, P.A., Michael, A., 2017. Cascadia subduction tremor muted by crustal faults. *Geology* 45 (6), 515–518. <https://doi.org/10.1130/G38835.1>.
- Wilson, D.S., 2002. The Juan de Fuca plate and slab: isochron structure and Cenozoic plate motions. In: Kirby, S., Wang, K., Dunlop, S. (Eds.), *The Cascadia Subduction Zone and Related Subduction Systems*, pp. 9–12.
- Zandt, G., Humphreys, E., 2008. Toroidal mantle flow through the western U.S. slab window. *Geology* 36, 295–298. <https://doi.org/10.1130/G24611A.1>.